Journal of Engineering Science and Technology
Vol. 5, No. 3 (2010) 361 - 372

THE INTERACTION OF A COLD ATOMISED SPRAY WITH A CIRCULAR CYLINDER

A. AROUSSI[1,*], N. LAD[2], M.F. MUHAMAD SAID[2],
D. ADEBAYO[2], M. AL-ATABI[3]

[1]Department of Mechanical Engineering, University Teknologi PETRONAS, Malaysia
[2]Thermo Fluids Group, University of Leicester, Leicester, UK
[3]School of Engineering, Taylor's University College, Malaysia

*Corresponding Author: aroussi@petronas.com.my

Abstract

The development of non-intrusive diagnostic techniques has significantly increased with the introduction of lasers. Laser based anemometry, such as Laser Doppler (LDA), Phase Doppler (PDA), and Particle Image Velocimetery (PIV) can provide an accurate description of flows without interference. This study determines experimentally the fluid motion resulting from the interaction of a liquid spray with a circular cylinder. Two experimental settings were examined: the first is a discharging spray into free air and the second is a spray impinging on a circular cylinder placed 25 cylinder diameters downstream of the nozzle. These sprays were quantified using PIV. A non-intrusive droplet sizing technique was used to characterise the spray. This has shown that, within the spray, the average droplet diameter increases when the circular cylinder is introduced and so does the frequency of occurrence of these large droplets. In the wake behind the cylinder, the smaller droplets were quickly entrained and recirculated, while the larger droplets continued in the general direction of the spray cone.

Keywords: Computational fluid dynamics, Particle image velocimetry, Circular cylinder, Droplet sizing.

1. Introduction

The flow interacting with a circular cylinder is of significant interest, due to its fundamental importance. For instance, it represents a generic configuration for studying vortex dynamics, the drag and lift variation due to wake unsteadiness, and it is relevant to a variety of engineering applications. These flow characteristics

Nomenclatures

A_p	Area of a particle, μm^2
D	Cylinder diameter, mm
D_p	Particle equivalent diameter, μm
Re	Reynolds number
U	Undisturbed velocity, m/s
U_{max}	Centreline velocity, m/s
We	Weber number

Abbriviations

LDA	Laser Doppler
PDA	Phase Doppler
PIV	Particle Image Velocimetery

have been investigated since the 1950's [1]. Early works of flow around a circular cylinder are provided by [2, 3], more recent computational studies by [4-6]. In these studies, the upstream flow was uniform.

In this study a spray gun was used to produce a multiphase flow at a Reynolds Number of 2400. Therefore the flow lies within the subcritical range [7]. In the subcritical range, at $10^3 < Re < 2\times10^5$, the flow around the cylinder is laminar and transition happens in the free shear-layer downstream of the cylinder. With increasing Reynolds number, the location of transition gradually moves upstream. For Reynolds numbers above $Re = 2\times10^5$, the location of transition has moved so far upstream that the boundary layer along the cylinder becomes partially turbulent. As a consequence, the boundary layer separation downstream is deferred, thereby reducing the size of the wake and, because of that, also the losses [8]. At Re = 3900, in the lower subcritical range, several experiments were performed by [9-12]. Details of these experiments are described in [13].

The purpose of this study is to determine, both experimentally and numerically, the intrusiveness of a cylindrical probe, such as an endoscope, within a multiphase flow. To quantify this intrusiveness, two experimental setups were examined. The first is a liquid-air blast atomiser discharging into free air. The second involves the introduction of a circular cylinder (representing a probe) placed 25 cylinder diameters downstream of the nozzle. The data obtained was collected using PIV and drop sizing.

2. Experimental Setup

To explore droplet transport around a circular cylinder, an experimental arrangement is used that provides a well-characterized homogeneous turbulent flow field around the obstacle. The experimental setup consists of non-swirling air flow that co-flows around the liquid injector. As shown in Fig. 1, the experiment is oriented horizontally, so that liquid droplets downstream of the obstacle hit a transparent screen protecting the laser, forming a film that runs down to a sump. The agent used in this study is water that was sprayed in the flow

field by either a 70° hollow cone or a 30° solid cone pressure-jet atomizer, as shown in Fig. 2. The absolute air pressure supplied to the atomiser is 345 kPa and the atomised air flow rate is 0.0045 kg/s.

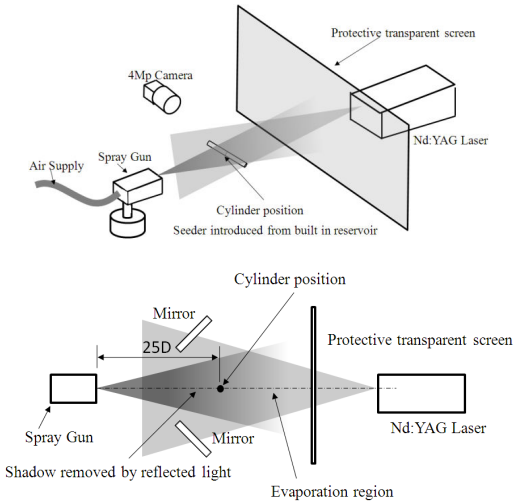

Fig. 1. Experimental Setup of the Spray System.

For these experiments, the incoming air, supplied from a 1.4×10^{-4} m^3/s compressor, was directly connected to the spray gun via a regulator valve. A flashlamp pumped, Nd:Yag double pulsed laser was used to produce a laser sheet 532 nm in wavelength. A four megapixel camera with a 60 mm lens was used to focus upon the particles of seeder illuminated by the laser sheet. The seeder utilised is Sphericel 50 μm (hollow glass spheres). This was added to the spray gun water supply bottle and is sprayed with the water. A circular cylinder of diameter D = 10 mm was positioned horizontally normal to the spray centreline 25D downstream of the spray nozzle. The position was controlled using a manual mechanical traverse system. This reduced the amount of positional error to ±0.1D.

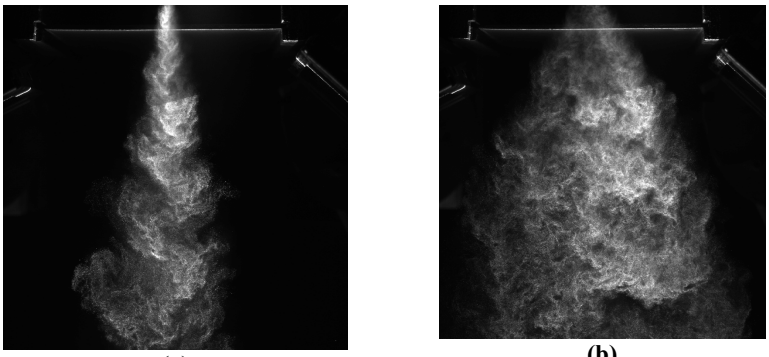

(a) **(b)**

Fig. 2. Raw Images of Spray from (a) Using a 30° Solid Cone and (b) A 70° Hollow Cone at the Nozzle Exit. Spray from Top to Bottom.

The laser control, the laser/camera synchronisation and the data acquisition and processing were handled by a hardware module and Dynamic Studio v1.45 software installed on 2.4 GHz quad core PC with 2 Gb of memory. The time interval between two laser pulses was equal to 15 μs. This allowed approximately a 25% particle displacement within a 32×32 pixel correlation grid. The trigger rate of the camera was set to 4 Hz and approximately 50 images were captured in each run. This value was used due to limitations in computational power when processing the images. The bottleneck of data transfer occurred at the hard disk buffer interface. The camera trigger captured images at a faster rate than the rate of data write on the hard disk. This was due to the camera being four megapixel producing a file size for each image capture of 6 Mb (12 Mb for each image pair). The image area was located 250 mm downstream of the nozzle exit, allowing a field of view of 140 mm × 160 mm. Recorded image pairs were correlated using a 32 × 32 pixel interrogation area with a 50% area overlap. The velocity vectors resulting from PIV are ensemble averages from 150 image pairs. 150 vector maps were used in the ensemble. Ideally, a larger ensemble would have been used to ensure statistical convergence, but it was not feasible to do so. The statistical convergence has been assessed by considering the statistics of an ensemble of 100 vector fields vs. an ensemble of 150 vector fields. The statistical convergence of the mean values of velocity profiles were calculated at various positions in the flow. The differences in the computed mean velocities between 100-frame and 150-frame ensembles are less than 4%.

Figure 3 shows the resulting ensemble average velocity vector maps. It shows that the 70° hollow cone significantly increases in jet cone angle with respect to the 30° solid cone. Figure 4 shows the raw image of the solid cone and the hollow cone sprays impinging on a cylinder. The velocity profiles in Figs. 5-8 were obtained from the ensemble average of the velocity vector maps from the cross correlation of image pairs like Fig. 4.

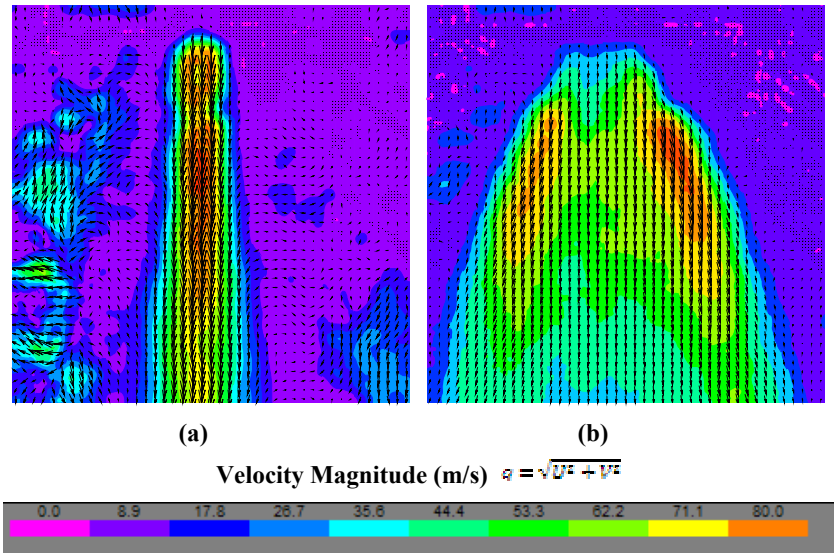

Fig. 3. Processed Time Averaged PIV Solutions for: (a) 30° Solid Cone, (b) 70° Hollow Cone. Iso-levels of Velocity Magnitude Show at the Nozzle Outflow.

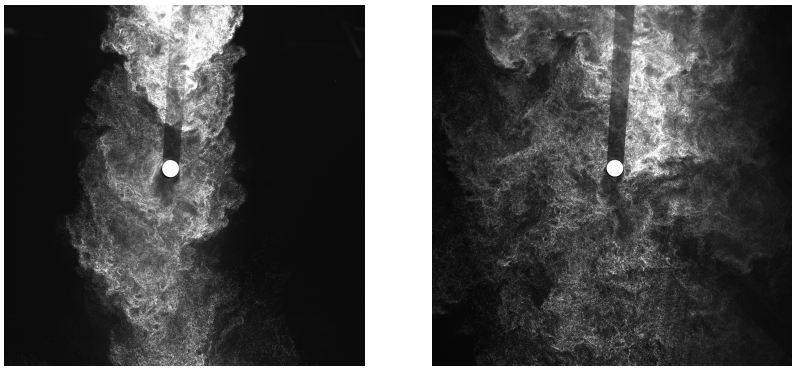

Fig. 4. Raw Images of Cylinder 25*D* Downsteam of the Nozzle in (a) 30 Degree Solid Cone Spray and (b) a 70 Degree Hollow Cone Spray. Spray Flow from Top to Bottom.

Figures 5-8 show that the droplets along the jet centreline are found to flow on the surface of the cylinder while those off-axis flow around or past the cylinder with an increased velocity. The droplets that impinge and wet the cylinder surface drip off at a rate of approximately one drop every three seconds. Some seeder was found to adhere to parts of the cylinder, the majority being collected at the trailing edge. Through the flow visualisation of Fig. 2, no evidence of secondary breakup of the droplets was observed. This was expected due to the low Weber number (We = 12) within the flow.

Figures 5-8 show the ensemble averaged PIV velocity profiles measured along the vertical plane aligned with the spray centreline, as shown in Fig. 1. The profiles are normalised by the spray centreline velocity, U_{max}, 20*D* downstream of the nozzle. Figures 5-8 show that introducing a circular cylinder of diameter $D = 10$ mm in the spray cone creates a noticeable impact on the mean flow. There is a noticeable rise in velocity as the spray is diverted around the body. Upstream of the cylinder, even though the image intensity is vastly diminished in the shadow of the cylinder, the presence of mirrors, located as shown in Fig. 1, enables larger droplets to still be identified. Figures 5-8 show that the upstream ensemble averaged velocity profiles with and without the cylinder are similar. The cylinder wake has a velocity defect of about 10% at 5*D* downstream of the cylinder, as shown by comparing the 5*D* profiles between Fig. 5 and Fig. 6. Similar results are obtained with the 70° hollow cone spray. The initial drop in momentum deficit is due to the reduction of the flow approach speed upstream of the cylinder. The reduction in flow speed is due to the increase in spray angle, which subsequently disperses much of the streamwise velocity into the *y* direction.

Figures 7 and 8 show velocity profiles that do not tend to zero at ±6 *y*/*D*, unlike Figs. 5 and 6. By inspecting the 70° hollow cone at the jet outlet, the cone has diverted most of the jet momentum off axis, resulting in the rise in downstream velocity measured in Figs. 7 and 8. Figures 7 and 8 have been obtained from the same field of view as that of Figs. 5 and 6. Due to the increased cone angle, the full spray width 25*D* downstream of the nozzle has not been captured in Figs. 7 and 8. The author has chosen not to increase the field of view for the hollow cone spray to keep the optical resolution of the spray around the

cylinder constant in all the experiments. Since the study is focused on the spray cylinder interaction in the area $-4 \leq y/D \leq 4$, the selected field of view was adequate to capture this interaction.

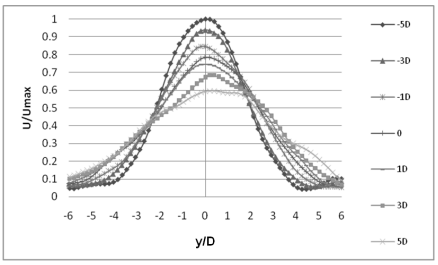

Fig. 5. 30° Solid Cone Spray without Cylinder. Normalised PIV Velocity Profiles.

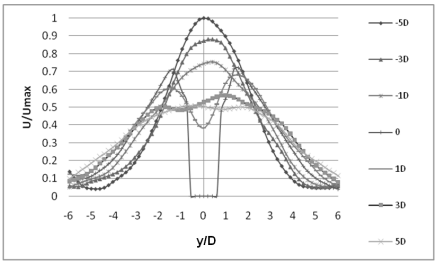

Fig. 6. 30° Solid Cone Spray with Cylinder. Normalised PIV Velocity Profiles.

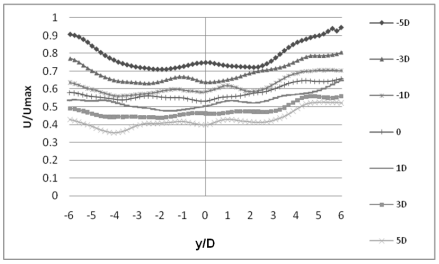

Fig. 7. 70° Hollow Cone Spray without Cylinder. Normalised PIV Velocity Profiles.

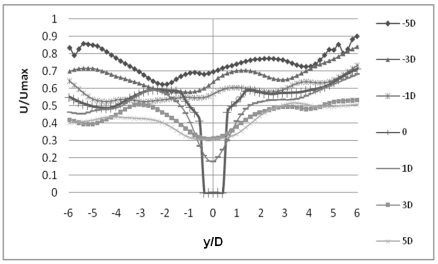

Fig. 8. 70° Hollow Cone spray with Cylinder. Normalised PIV Velocity Profiles.

3. Drop Size Analysis

Spray characterisation was carried out using an in-house method based on a non-intrusive image processing technique. The hardware layout for this technique is illustrated in Fig. 9. The drops in the spray are illuminated with a pulsed laser of 532 nm wavelength. The light scattered by the drops is recorded using a digital camera in a sequence of frames. Images acquired by the camera are then directly transferred from the camera to the memory of the host computer for image processing. The images are analysed using in-house drop size measurement software to obtain the spray drop size distribution.

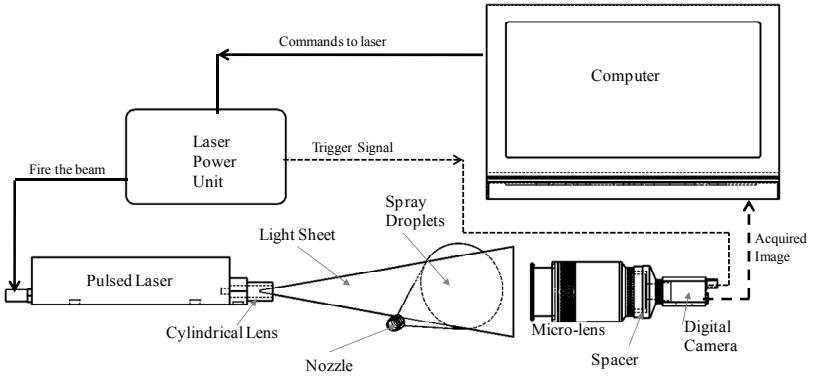

Fig. 9. Instrumentation Setup for the Droplet Size Analysis.

Once the raw image is received by the software, it is processed to enhance its appearance and then analysed to extract the particle size distribution. The image analysis software was written in LabView. The flowchart of the algorithms is outlined in Fig. 10. After image acquisition, the first processing stage is image enhancement. It is the process by which the acquired images are improved [14]. In this study, the approach is to enhance each image by changing the brightness, contrast and the gamma distribution. A filter function is also applied to each image background in order to correct for the non-uniform light scattering intensity of the laser sheet used to illuminate the field of view.

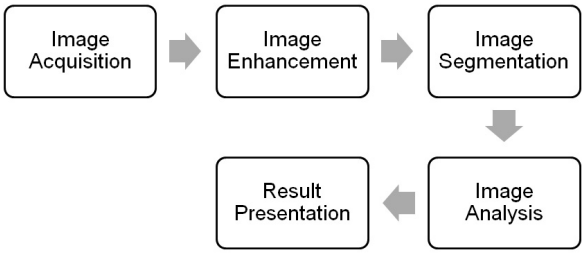

Fig. 10. Digital Drop Size Analysis Flowchart.

The second stage of image processing is image segmentation. The particle outlines in the image are used to divide the image into regions which are made up of pixels. In this case, thresholding is used to separate the particle outlines from the image

background. In order to obtain the area of a single particle, the number of pixels that represent a single bright object is calculated. This algorithm also determines the number of particles in each image. The particle diameter is then computed based on the area of each particle. In this case, the calculation of particle size is based on the particle equivalent diameter D_p defined in the following equation

$$D_p = 2\sqrt{\frac{A_p}{\pi}}$$

where A_p is the area of the particle. The number frequency of the particle size data in each image is determined using constant bin widths of 2 μm over the particle size range 10 μm to 30 μm.

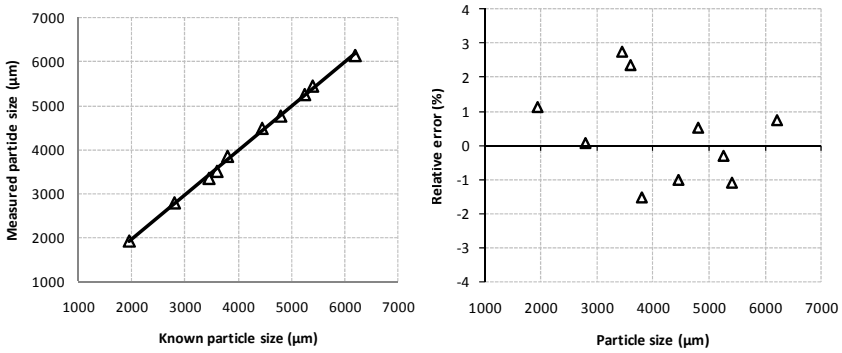

(a) **(b)**

Fig. 11 (a) Direct Comparison between Measured and Known Particle Size, (b) Relative Error of Particle Size Measurement.

Static images were used for calibration and to assess the absolute accuracy of the in-house method. The camera was positioned over particles of known size placed on a flat surface. A check-board was laid on the surface to transform pixel coordinates to real-world coordinates through scaling in the x and y (horizontal and vertical) directions. In this study, polystyrene particles of known size were used for the calibration. The relationship between the measured and known particle sizes is shown in Fig. 11(a). The in-house method is shown to detect the size of the test particles with good linearity with a ratio of 1:1. From the data in Fig. 11(a), the relative percentage error in particle size measurement was determined. This is shown in Fig. 11(b). The majority of the particles are measured within ±2.0% of their known diameter. It was found that the relative error reduced with increasing particle size.

The measurements of atomised water drops from a spray nozzle were obtained on different cross-flow planes normal to the spray axis, located as stated in Table 1. Each plane is surveyed five times.

Table 1. Particle Sizing Cross-flow Planes.

Cases	Point of Measurement
Upstream	23D from nozzle exit
Downstream	27D from nozzle exit
Downstream (with Probe)	27D from nozzle exit

In the present system, the camera acquires 50 real-time images with a resolution of 1280×960 pixels for each test. A micro-lens is used to focus the camera on the light sheet. A sample of an image acquired by the camera and processed by the software is shown in Fig. 12. The selected measurement cross-planes are sufficiently downstream from the nozzle exit to give non-overlapping spray drops in the small field of view of 3 mm x 2 mm. Some of the droplet images in Fig. 12 (left) are blurred due to the drops moving out of focus. In order to determine an accurate drop size distribution, only the fully illuminated drops are retained in Fig. 12 (right). In the processed image, the size of each drop is determined by the image segmentation and image analysis steps of Fig. 10.

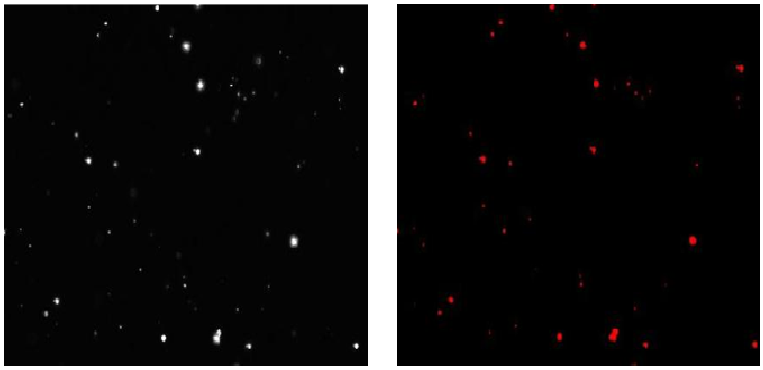

Fig. 12. Acquired Image (left) and Processed Image (right).

Figure 13 shows that the drop size distribution for three different cases of Table 1 is broadly similar.

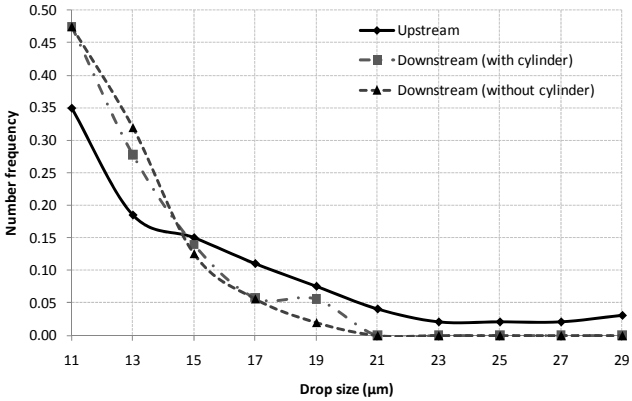

Fig. 13. Drop Size Distribution for Three Different Cases.

For each configuration, the drop size measurement from five tests has been ensemble averaged to obtain the mean drop size reported in Fig. 14. The dominant drop size in this spray system over the measured range, 10 μm to 30 μm, is 11μm ± 1μm with a number frequency of 0.35 to 0.48. Figure 14 shows that the measured average drop size downstream of the cylinder over the

particle size range 10 μm to 30 μm is lower than upstream of it. The lower value of the average drop size is believed to be due to spray break-up. When the cylinder is placed in the spray system, the measured drop size is found to be higher than without probe. This is probably due to the coalescence of the drops as they flow around the cylinder. The coalescence occurs mainly at the wake re-attachment zone approximately 1.5*D* downstream of the cylinder. This is recognised by the sudden increase of illumination intensity of a localised area after a darkened wake area where droplets sparse. The increase in intensity is due to the convergence of particles from either side of the wake increasing the density of droplets in the area. The clustering of droplets increase the amount of light energy scattered.

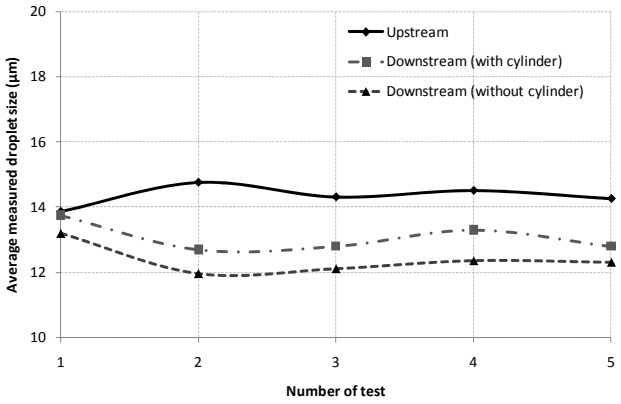

Fig. 14. Comparison of Measured Drop Size on Three Different Cases.

Based on the five tests that were carried out on each of the three configurations stated in Table 1, the standard deviation has been plotted to show that repeatability of each test. Figure 15 shows that the drop size standard deviation is lower than 7%.

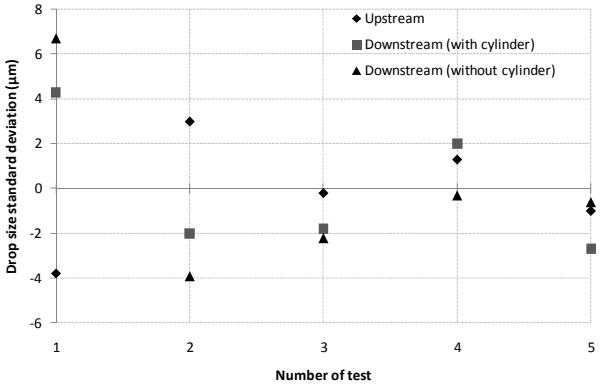

Fig. 15. Standard Deviation of Measured Drop Size.

4. Conclusion

The interaction of a circular cylinder with an atomised spray flow has been studied within this paper. Non intrusive optical measurement techniques have been used to characterise the flow velocity and measure droplet size both upstream and downstream of the circular cylinder. Ensemble averaged PIV vector maps were analysed to provide velocity data at increasing displacements from the nozzle exit. The difference between the vector maps with and without the cylinder expressed as velocity defect quantifies the intrusiveness of the cylinder in the spray flow. This study observed a 38% velocity deficit at 1*D* downstream of the circular cylinder within a 30° solid cone atomised spray. The velocity deficit reduced to 16% and 10% at 3*D* and 5*D* downstream respectively. The deficit experienced within the 70° hollow cone spray is initially lowered at 31% at 1*D*. Further downstream the deficit values are 17% and 10% at 3*D* and 5*D* downstream respectively. Using the droplet size technique it is observed that, probably due to the coalescence of the drops overflowing the cylinder, the mean drop size downstream of the cylinder is slightly larger than without the cylinder. This paper can therefore confirm experimentally that the presence of an optical measurement device, such as an endoscope, does not only have an effect on velocity magnitude and direction but also on droplet sizing. It must be recognised that careful consideration must be undertaken to ensure that the error created by semi-intrusive imaging is counted for or reduced.

References

1. Roshko, A. (1954). On the development of turbulent wakes from vortex streets. National Advisory Committee for Aeronautics, NACA Report 1191.
2. Hinze, J.O. (1975). *Turbulence*. (2nd Ed.), New York: McGraw Hill Companies.
3. Schlichting, H. (1979). *Boundary-layer theory*. (7th Ed.), New York: McGraw Hill Inc.
4. Breuer, M. (1998). Large eddy simulation of the subcritical flow past a circular cylinder: numerical and modeling aspects. *International Journal for Numerical Methods in Fluids*, 28(9), 1281-1302.
5. Kravchenko, G.A.; and P. Moin (2000). Numerical studies of flow over a circular cylinder at $Re_D = 3900$. *Physics of Fluids*, 12(2), 403-417.
6. Travin, A.; Shur, M.; Strelets, M.; and Spalart, P. (1999). Detached-eddy simulations past a circular cylinder. *Flow, Turbulence and Combustion*, 63(1-4), 293-313.
7. Zdravkovich, M.M. (1997). *Flow around circular cylinders, Vol. 1: Fundamentals*. Oxford University Press, USA.
8. Wissink, J.G.; and Rodi, W. (2008). Numerical study of the near wake of a circular cylinder. *International Journal of Heat and Fluid Flow*, 29(4), 1060-1070.
9. Dong, S.; Karniadakis, G.E.; Ekmekci, A.; and Rockwell, D. (2006). A combined direct numerical simulation-particle image velocimetry study of the turbulent near wake. *Journal of Fluid Mechanics*, 569, 185-207.

10. Lourenco, L.M.; and Shih, C. (1993). Characteristics of the plane turbulence near wake of a circular cylinder, a particle image velocimetry study. Published in Beauden and Moin (1994), Data taken from Kravchenko and Moin (2000) [5].
11. Norberg, C. (1994). An experimental investigation of flow around a circular cylinder: influence of aspect ratio. *Journal of Fluid Mechanics*, 258, 287-316.
12. Ong, L.; and Wallace, J. (1995). The velocity field of the turbulent very near wake of a circular cylinder. *Experiment in Fluids*, 20(6), 411-453.
13. Norberg, C. (2003). Fluctuating lift on a circular cylinder: review and new measurements. *Journal of Fluids and Structures*, 17(1), 57-96.
14. Petrou, M.; and Bosdogianni, P. (1999). *Image Processing: The Fundamentals*: Wiley.